Supplementary Information for

Anthropogenically Induced Shift to Labile Phytoplankton-Derived Carbon Undermines Lake Carbon Burial Efficiency

Tiangang Tang[1,2], Wei Zhang[1,2*], Zhanxiang He[1,2,6], Yang Gao[3], Qing Zhu[4], Gan Zhang[5], Peilei Hu[1,2], Pengpeng Duan[1,2], Xinyi Yang[1,2], Hanqing Wu[1,2], Dan Xiao[1,2], Jun Xiao[1,2], Xiangkun Qi[1,2], Hongsong Chen[1,2], Kelin Wang[1,2*]

[1] Institute of Subtropical Agriculture, Chinese Academy of Sciences, Changsha, China

[2] Huanjiang Agriculture Ecosystem Observation and Research Station of Guangxi, Guangxi Key Laboratory of Karst Ecological Processes and Services, Huanjiang Observation and Research Station for Karst Ecosystems, Chinese Academy of Sciences, Huanjiang, Guangxi, China

[3] Key Laboratory of Ecosystem Network Observation and Modeling, Institute of Geographic Sciences and Natural Resources Research, Chinese Academy of Sciences, Beijing, China

[4] State Key Laboratory of Lake and Watershed Science for Water Security, Nanjing Institute of Geography and Limnology, Chinese Academy of Sciences, Nanjing, China

[5] State Key Laboratory of Advanced Environmental Technology, Guangzhou Institute of Geochemistry, Chinese Academy of Sciences, Guangzhou, China

[6] University of Chinese Academy of Sciences, Beijing, China

Contents

Text S2. First-Order Kinetic Mineralization Model

Supplementary Figures (Figs. S1 – S16)

Supplementary Tables (Tables S1 – S2)

Supplementary References

Text S1. Bayesian Isotope Mixing Model for Source Apportionment

A Bayesian stable isotope mixing model was employed to quantitatively apportion the contributions of potential sources to sedimentary *n*-alkanes[1,2]. This approach integrates compound-specific dual-isotope ($\delta^{13}C$ and $\delta^{2}H$) signatures within a probabilistic framework to estimate source proportions. It provides a robust tool for resolving source mixtures in complex environmental systems. The model relies on the principle of isotopic mass balance, whereby the isotopic composition of a mixture is expressed as the weighted sum of contributions from distinct sources. Within a Bayesian framework, prior information (e.g., source isotopic ranges) can be incorporated, yielding posterior probability distributions for source contributions that explicitly quantify estimation uncertainty. Analyses were performed using the MixSIAR package in R, a widely adopted tool for such applications (https://github.com/brianstock/MixSIAR).

S1.1 Rationale for a Dynamic End-Member Approach

In geochemical studies, mid-chain *n*-alkanes (nC_{23}/nC_{25}) have commonly been

used as biomarkers for aquatic macrophytes. However, recent research has questioned the specificity of this indicator. Terrestrial plants can contribute a notable proportion (~10%) of mid-chain homologues to their *n*-alkane profile, and their overall alkane abundance typically far exceeds that of aquatic vegetation[3,4]. Moreover, fossil fuel combustion emits mid-chain *n*-alkanes, further complicating source interpretation. Evidence from our study systems includes: (i) sustained accumulation of mid-chain *n*-alkanes in Lake Erhai despite documented macrophyte decline[5]; (ii) low odd-over-even predominance (OEP) values[6,7] (EH ~4.21, CH ~2.76, < 5 indicate mixed origins, potentially including fossil sources); and (iii) a shift in $\varepsilon^2H_{C29/C23}$ from positive (aquatic-like) to negative (terrestrial-like) values in EH, accompanied by a depletion trend in CH[8] (Fig. S7). Traditional isotope mixing models often apply static modern end-member values to historical samples, thereby ignoring temporal changes in environmental isotopic baselines[9–11] (e.g., precipitation δ^2H, lake water δ^2H, and DIC $\delta^{13}C$). This assumption can introduce substantial apportionment errors.

Our primary goal was to reconstruct the relative contributions of aquatic macrophytes, terrestrial plants, and fossil fuels to mid-chain *n*-alkanes (nC_{23}/nC_{25}). Given clear evidence of mixed sources, we constructed layer-specific end-members using isotopic signals preserved in the sediment record itself, thereby capturing historical environmental conditions.

S1.2 End-Member Derivation

We defined three sources: fossil fuels, aquatic macrophytes, and terrestrial plants.

Fossil fuel end-members. The isotopic composition of n-alkanes emitted during fossil fuel combustion varies with fuel type (e.g., coal, petroleum) and combustion conditions, rendering direct inference of petrogenic signatures in sediments challenging[12–15]. Atmospheric intermediate-volatility n-alkanes primarily originate from fossil fuel emissions. After atmospheric mixing and transport, they enter watersheds via dry/wet deposition and are ultimately incorporated into lake sediments through hydrological processes, providing an integrated regional signal of fossil fuel combustion. Accordingly, we adopted the mean isotopic signature of atmospheric intermediate-volatility n-alkanes as the fossil source end-member[16]: $\delta^{13}C = -28.0 \pm 1.5$ ‰, $\delta^{2}H = -100 \pm 15$ ‰.

Terrestrial plant end-member. Sedimentary nC$_{29}$ is predominantly derived from terrestrial plants and thus serves as a direct recorder of past terrestrial plant wax $\delta^{2}H$[17,18]. To estimate the $\delta^{2}H$ value of terrestrial-derived nC$_{23}$, we applied a mean chain-length hydrogen isotope fractionation factor $\varepsilon^{2}H_{C29/C23} = -27.3 \pm 20.0$ ‰, synthesized from published measurements across diverse plant types (herbs, gymnosperms, and angiosperms)[8]. For $\delta^{13}C$, we accounted for the minor but consistent depletion with increasing chain length in terrestrial plants[19], using $\varepsilon^{13}C_{C29/C23} = 1.5$ ‰.

Aquatic macrophyte end-member. The $\delta^{2}H$ signature of aquatic macrophyte n-alkanes is primarily controlled by lake water $\delta^{2}H$ [20–22]. We used sedimentary nC$_{17}$ $\delta^{2}H$ as a robust proxy for past lake water $\delta^{2}H$. Literature compilations indicate that hydrogen isotope fractionation between lake water and sedimentary nC$_{17}$ is relatively constant.

Our surface-sediment analyses from Lakes Erhai and Chenghai showed fractionation from the annual mean lake water δ^2H (–154.8‰) consistent with values reported for lakes in the Americas (–166.6‰) and Europe (–149.1‰) [23,24] (Fig. S8a). Critically, the fractionation between lake water and aquatic macrophyte $nC_{23/25}$ is of similar magnitude. Therefore, we directly applied the measured sedimentary nC_{17} δ^2H as the δ^2H end-member for aquatic $nC_{23/25}$. For $\delta^{13}C$, values in large aquatic plants (primarily submerged macrophytes) are mainly governed by the $\delta^{13}C$ of dissolved inorganic carbon (DIC)[25]. Sediment inorganic carbon (IC) $\delta^{13}C$, controlled by boundary-layer thickness and DIC $\delta^{13}C$[26], remained stable in both lakes (EH: –3.0 ± 0.6‰; CH: –2.6 ± 0.6‰; Fig. S8b), indicating minimal historical variation in the DIC pool utilized by aquatic plants for photosynthesis. Consequently, we used the mean $\delta^{13}C$ value of modern regional aquatic plant $nC_{23/25}$ (–22.7 ± 2.0‰) as the historical end-member.

End-member values for nC_{25} were subsequently derived from those for nC_{23}, assuming consistent isotopic offsets between homologues[17,19], with nC_{25} enriched by ~5‰ in $\delta^{13}C$ and ~0.5‰ in δ^2H relative to nC_{23}.

S1.3 Model Execution, Diagnostics and Validation

Models were run using Markov Chain Monte Carlo (MCMC) sampling with 300,000 iterations, a burn-in of 200,000, and a thinning interval of 100. The δ^2H and $\delta^{13}C$ values of $nC_{23/25}$ served as the mixture data (Fig. S9). Layer-specific end-member values and associated uncertainties (20.0‰ for δ^2H, 2.0‰ for $\delta^{13}C$) were used as source data. Convergence was confirmed by Gelman–Rubin diagnostics (all <1.05). An

uninformative Dirichlet prior with parameters (1,1,1) was specified for source proportions to minimize prior influence and allow the data to dominate the posterior estimates. To verify this setup, prior distributions were visualized using the 'plot_prior' function in MixSIAR. As illustrated for EH nC_{23} (Fig. S10), the user-specified prior (left panels, blue) matches the default uninformative prior (right panels, red), with marginal distributions showing the characteristic decline from low to high proportions—consistent with a uniform prior over the simplex. This confirms the neutrality and appropriateness of the model assumptions for the present study. The effectiveness of source separation is further validated by (i) the strengthened correlation between the model-derived terrestrial-sourced mid-chain *n*-alkane pool and the unambiguous long-chain *n*-alkane pool (Fig. S11), and (ii) the close agreement between the reconstructed decline in aquatic macrophyte OC and independent historical records of macrophyte coverage in Lake Erhai (Fig. S12).

Text S2. First-Order kinetic Mineralization Model

We developed a first-order kinetic mineralization model based on organic carbon (OC) source classification to quantitatively simulate the dynamic burial and mineralization processes of OC in lake sediments. The model is constructed within the theoretical framework of the "deposition–transformation–burial" carbon cycle and extends the core mechanism of the Dynamic Mineralization and Storage of Organic Carbon (DMSOC) model proposed by Jiang et al. [27].

S2.1 Theoretical Basis and Logical Framework

The long-term preserved OC in sediments is not simply the initial deposited amount, but rather the net result of continuous mineralization and the differential stability of carbon from distinct sources. Traditional approaches that estimate carbon sequestration solely from measured total OC content overlook the dynamic changes in both the composition and total stock of the carbon pool during diagenetic mineralization.

To address this limitation, our model follows a clear logical sequence:

a. Source Apportionment: Source-specific biomarkers (*n*-alkanes) are first used to reconstruct historical input fluxes of OC from different sources. This serves as the foundation for dynamic simulation.

b. Initial Carbon Pool Quantification: Biomarker fluxes are converted into initial depositional masses of each OC type using source-specific conversion factors. This step bridges microscopic biomarkers to the macroscopic carbon pool.

c. Kinetic Mineralization Simulation: Because OC from different sources exhibits distinct chemical compositions and bioavailabilities, separate first-order kinetic equations with source-specific parameters are applied to simulate post-depositional decay.

d. Residual Carbon Pool Integration: The remaining OC from each source after a given burial period is summed to obtain the theoretical total OC content of a sediment layer at the time of sampling, allowing direct comparison and validation against measured values.

This framework transforms the static concept of a "carbon pool" into a dynamic "carbon flow" process, enabling quantitative assessment of long-term carbon burial efficiency and sink functionality.

S2.2 Mathematical Expression and Mechanistic Rationale

The core equation of the model predicts the total remaining OC content, $OC_{predicted}$, in a sediment layer after a burial time *t*:

$$OC_{predicted} = \sum\left[Source_i \times d_i \times (1 - m_i) + Source_i \times d_i \times m_i \times \left(1 - exp(-k_i \times t)\right)\right]$$

where the subscript *i* denotes the three OC sources: phytoplankton (Alg), aquatic macrophytes (Aqu), and terrestrial plants (Ter). The parameters and their mechanistic interpretations are as follows:

$Source_i$ – Source Source-Specific Input Flux ($mg \cdot m^{-2} \cdot yr^{-1}$): The time-dependent driver of the model, reconstructed from down-core concentration profiles of diagnostic n-alkanes (Bio-*n*C_{17} for algae, Aqu-*n*Alk for aquatic plants, and Ter-*n*Alk for terrestrial plants).

di – Biomarker-to-OC Conversion Coefficient (g OC per μg biomarker): This source-specific coefficient converts biomarker flux into initial depositional OC flux. It reflects differences in lipid synthesis efficiency and the proportional contribution of lipids to total organic matter among sources (e.g., algae typically yield higher *di* values than terrestrial plants). The parameter is calibrated during model optimization.

m_i – Maximum Mineralizable Fraction (dimensionless, 0–1): The proportion of OC from source *i* that is theoretically susceptible to microbial decomposition. The

remaining fraction ($1-m_i$) is considered recalcitrant or inert on centennial timescales and may contribute to long-term geological carbon storage (e.g., kerogen precursors). For example, terrestrial OC, rich in refractory compounds like lignin, typically has a lower m_i value than labile algal OC.

k_i – First-Order Decay Constant (yr^{-1}): The kinetic parameter governing the decomposition rate of the mineralizable OC pool ($m_i \times d_i \times Source_i$). The term $\exp(-k_i \cdot t)$ describes the exponential decay of this reactive carbon pool with burial time. higher *ki* values indicate faster mineralization. Differences in k_i among sources reflect variations in molecular complexity and degradability, typically following the order: algae > aquatic macrophytes > terrestrial plants.

t– Burial Time (years): The age of each sediment layer, determined by ^{210}Pb dating using the constant rate of supply (CRS) model (Fig. S2).

S2.3 Key Model Assumptions

Validity of Source Classification: The selected *n*-alkane biomarkers can effectively distinguish and quantify these three primary OC sources, and they are relatively stable during early diagenesis, preserving source information.

Applicability of First-Order Kinetics: On a centennial timescale, the mineralization rate of the reactive OC component from each source is proportional to its standing stock, conforming to first-order reaction kinetics—a common assumption in sedimentary organic matter degradation studies.

Spatiotemporal Homogeneity of Parameters: Within the studied time frame and

spatial scope (similar lake types), the degradation characteristics (m_i, k_i) and biomarker significance (d_i) of OC from the same source remain essentially constant. This assumption allows us to simulate the historical process of the entire sediment core using a single set of parameters.

Independence of Processes: The mineralization processes of OC from different sources are independent; significant interactive effects, such as strong priming effects on mineralization rates, are not considered in this version.

Through this mathematical framework and mechanistic setup, the model integrates dating data, biomarker indices, and measured total OC to reconstruct the historical dynamics of OC deposition and mineralization, thereby enabling an assessment of long-term carbon burial efficiency.

S2.4 Optimized Parameters and Model Performance

The nine unknown parameters (d_{alg}, m_{alg}, k_{alg}, d_{aqu}, m_{aqu}, k_{aqu}, d_{ter}, m_{ter}, k_{ter}) were simultaneously optimized by minimizing the sum of squared residuals between the measured OC profile and the modeled $OC_{predicted}$ profile for the combined 110 data points from both lakes, using the 'nls' function in R. The optimization was constrained such that[27], $d_{alg} > d_{aqu} > d_{ter}$; $m_{aqu} > m_{alg} > m_{ter}$; $k_{alg} > k_{aqu} > k_{ter}$.

The optimized parameters are:

Phytoplankton: m_{alg} = 0.94, k_{alg} = 1.35 yr^{-1}, d_{alg} = 70.2 g OC per μg Bio-*n*C_{17}.

Aquatic macrophyte: m_{aqu} = 0.96, k_{aqu} = 0.40 yr^{-1}, d_{aqu}= 36.1 g OC per μg Aqu-*n*Alk.

Terrestrial plant: m_{ter} = 0.79, k_{ter} = 0.14 yr^{-1}, d_{ter} = 4.9 g OC per μg Ter-*n*Alk.

The model explained 70.9% of the variance in observed OC (adjusted R^2 = 0.683,). Key performance metrics include: Nash-Sutcliffe Efficiency (NSE) = 0.709, Root Mean Square Error (RMSE) = 3.42 mg g^{-1}, Mean Absolute Error (MAE) = 2.77 mg g^{-1}, and Bias = –0.08 mg g^{-1}. Residuals were normally distributed (Shapiro-Wilk p = 0.87).

To evaluate the robustness of burial efficiency (BE) trends to parameter uncertainty, we conducted a sensitivity analysis by independently perturbing each of the nine parameters by ±1%. The maximum change in predicted OC for any sample was less than 5%. This confirms that although absolute $OC_{predicted}$ values are parameter-dependent, the relative temporal and spatial trends in BE—central to our mechanistic interpretations—are highly robust. Detailed diagnostics are presented in Fig. S14 and summarized in Table S1.

Supplementary Figures (Figure S1 – S13)

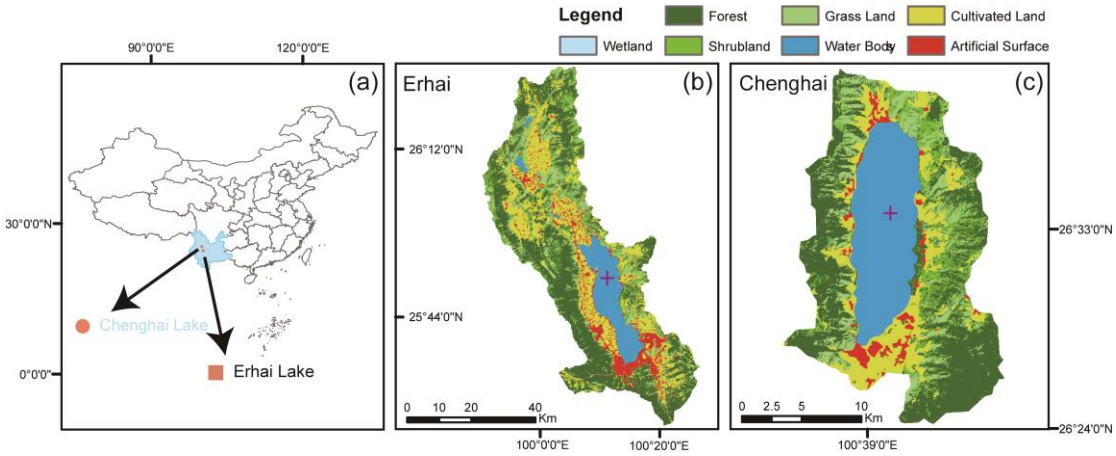

Figure S1. Study area and sampling sites. (a) Location of Lake Erhai and Lake Chenghai on the Yunnan-Guizhou Plateau, Southwest China. (b, c) Schematic land-use context of the Erhai and Chenghai drainage basins, respectively. The cross indicates the sediment coring location at the deepest point of each lake.

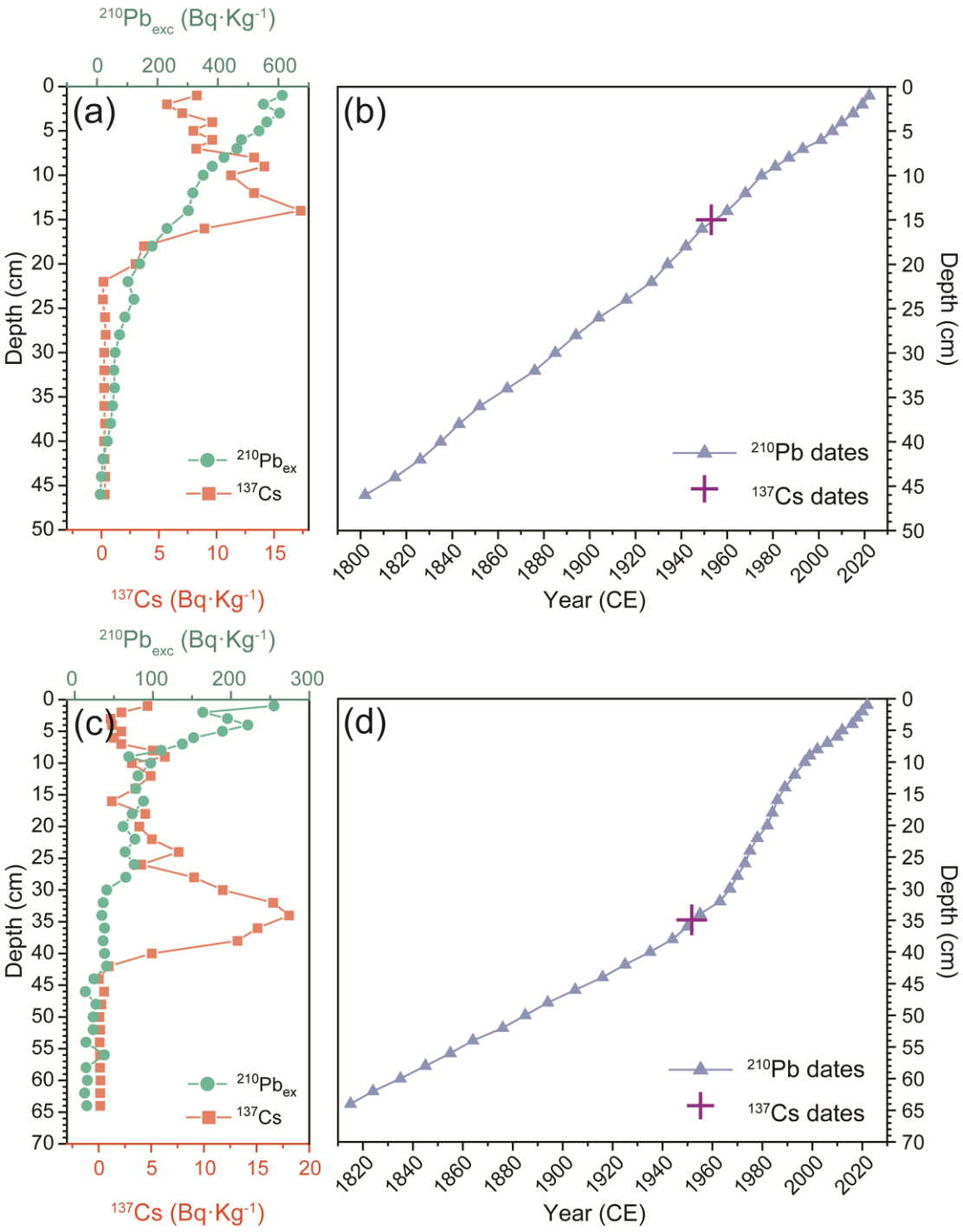

Figure S2. Radionuclide profiles and age-depth models for Lake Erhai and Lake Chenghai sediment cores. (a, c) Down-core distributions of unsupported ^{210}Pb ($^{210}Pb_{exc}$, green circles) and ^{137}Cs (yellow triangles) activities in the Erhai (EH) and Chenghai (CH) cores. (b, d) Corresponding age-depth models established using the Constant Rate of Supply (CRS) model. The ^{137}Cs peak (1963) is marked with a cross for validation.

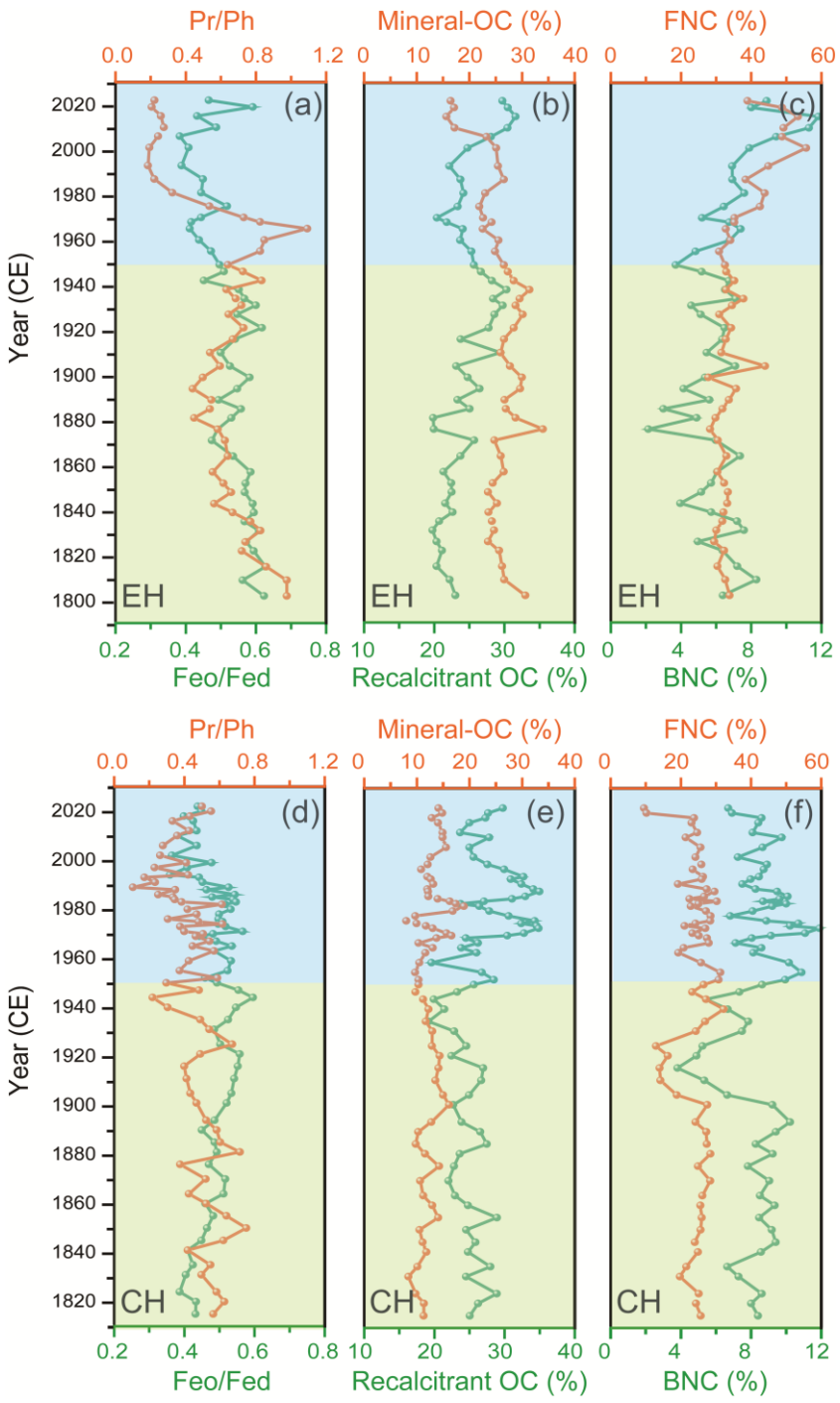

Figure S3. Temporal variations of sedimentary preservation-condition indicators. (a-c) Down-core profiles for Erhai: (a) redox indicators (Feo/Fed; Pr/Ph), (b) protection indicators (RCP; Mineral-OC), (c) proportion of microbial necromass carbon to OC (BNC; FNC). (d-f) Corresponding profiles for Chenghai. Abbreviations: BNC, bacterial necromass carbon fraction; FNC, fungal necromass carbon fraction; Feo/Fed, reactive free iron to total free iron ratio; Pr/Ph, Pristane/Phytane ratio; RCP, proportion of recalcitrant carbon pool; Mineral-OC, mineral-associated

241 organic carbon. Shaded bands represent the three anthropogenic phases defined in the main text.

242

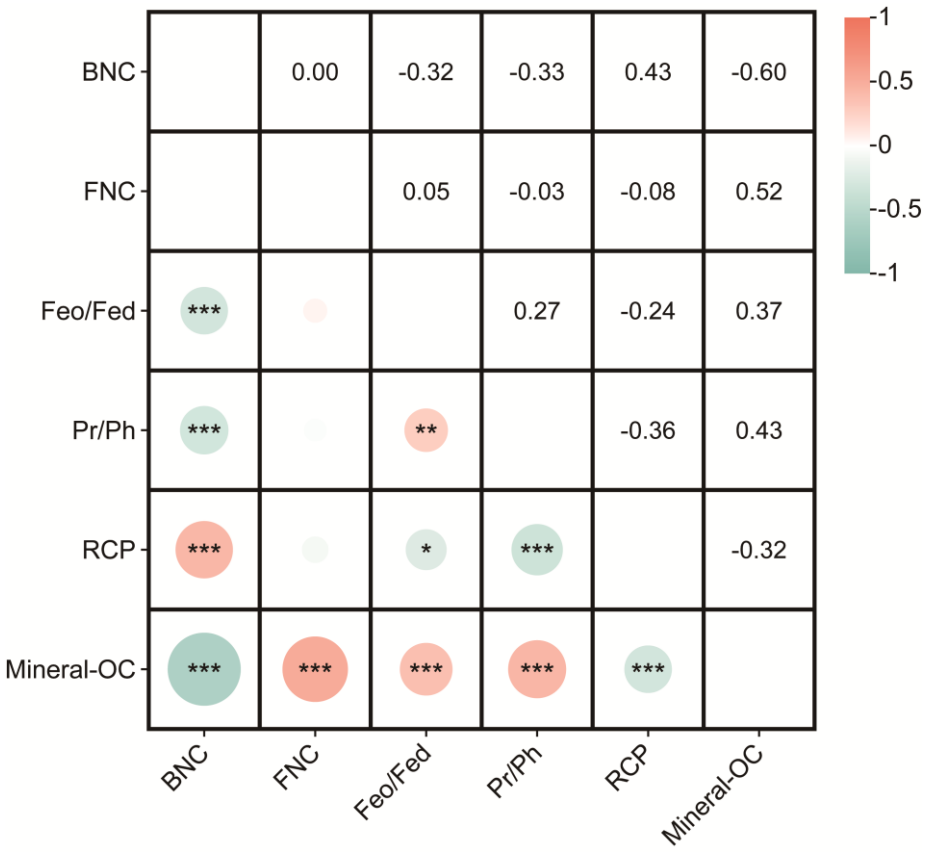

243

244 **Figure S4. Linear correlation matrix of sedimentary parameters in cores from Lakes Erhai**
245 **and Chenghai.** Abbreviations: BNC, bacterial necromass carbon fraction; FNC, fungal necromass
246 carbon fraction; Feo/Fed, reactive free iron to total free iron ratio; Pr/Ph, Pristane/Phytane ratio;
247 RCP, proportion of recalcitrant carbon pool; Mineral-OC, mineral-associated organic carbon.
248 Asterisks denote statistical significance (*$p < 0.05$, **$p < 0.01$, ***$p < 0.001$).

249

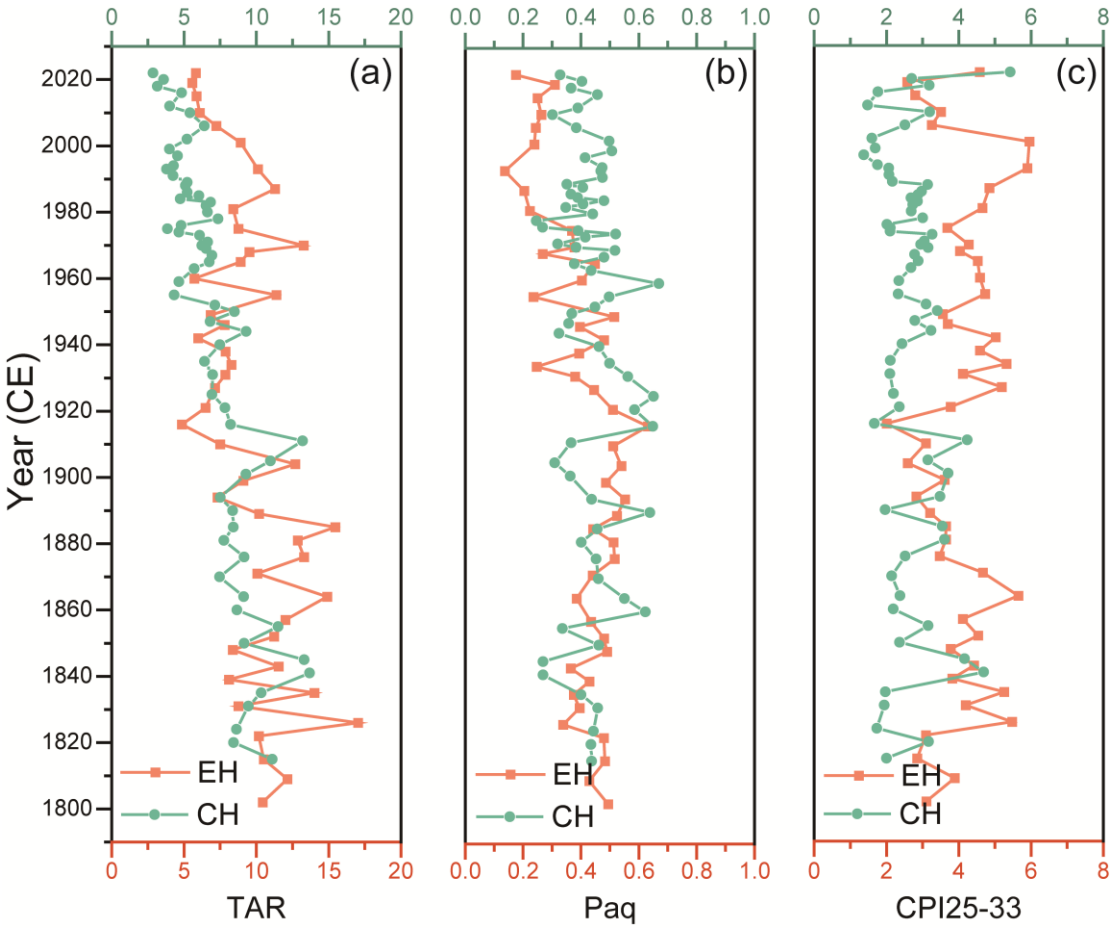

Figure S5. Down-core distributions of n-alkane source proxies in sediments from Lakes Erhai (EH) and Chenghai (CH). (a) Decreasing terrestrial-to-aquatic ratio (TAR) toward the present, consistent with increasing phytoplankton contributions over time. (b) Decline in the Paq index in recent EH sediments, indicating a reduction in aquatic macrophyte inputs. (c) Low carbon preference index ($CPI_{25–33}$) values, suggesting the influence of fossil-fuel contamination and/or early diagenetic alteration.

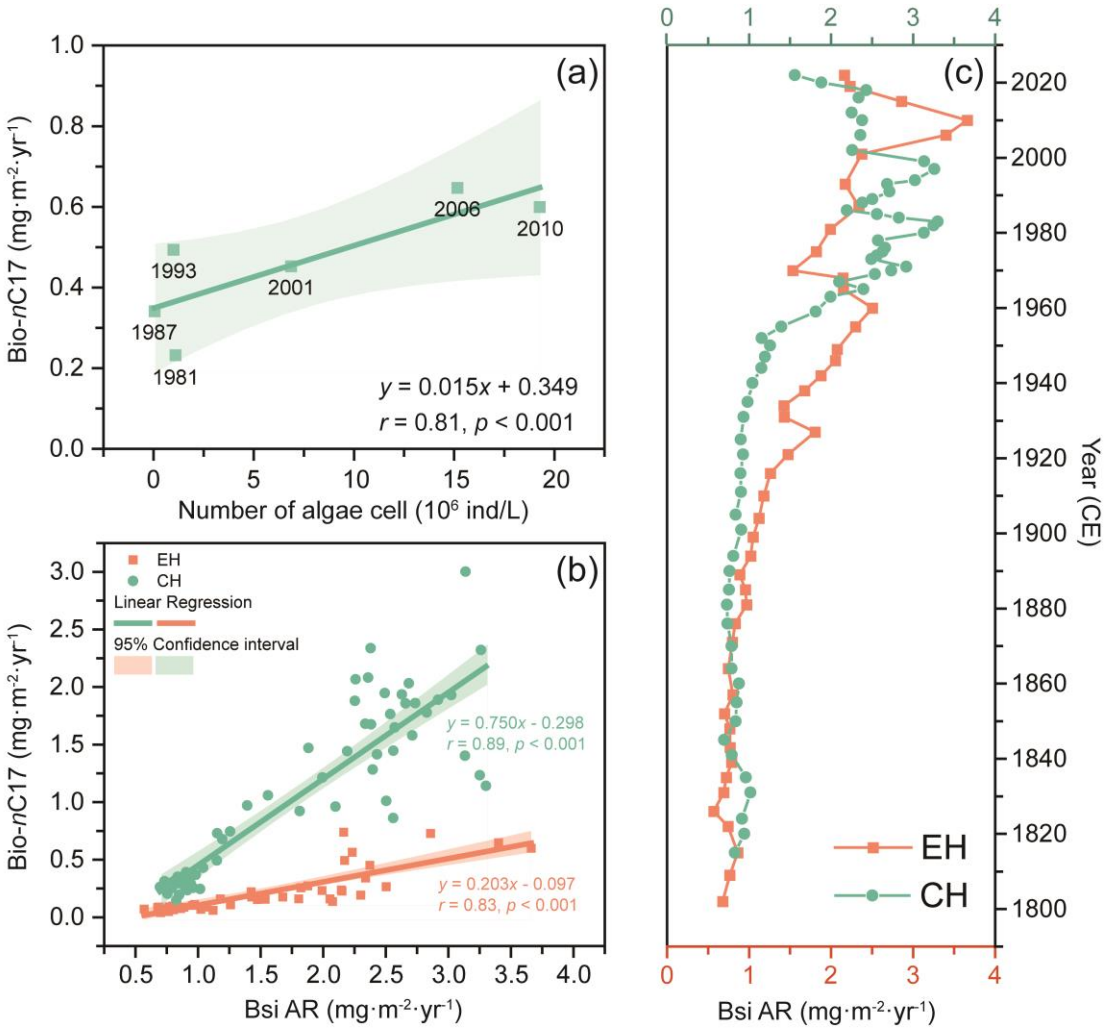

Figure S6. Multi-proxy validation of the phytoplankton biomarker Bio-*n*C$_{17}$. (a) Biogenic silica accumulation rate (BSi AR) in Lakes Erhai (EH) and Chenghai (CH). Values remain low and stable over time (coefficient of variation ~ 0.5), with only minor fluctuations after 1950 (EH) and 1920 (CH). (b) Strong positive correlation between Bio-*n*C$_{17}$ AR and BSi AR in both lakes (EH: $r = 0.83$; CH: $r = 0.89$; $p < 0.001$). (c) Significant correlation between modern phytoplankton biomass (instrumental record) and sedimentary Bio-*n*C$_{17}$ AR in Lake Erhai ($r = 0.81$, $p < 0.001$), with points labeled by sediment burial year.

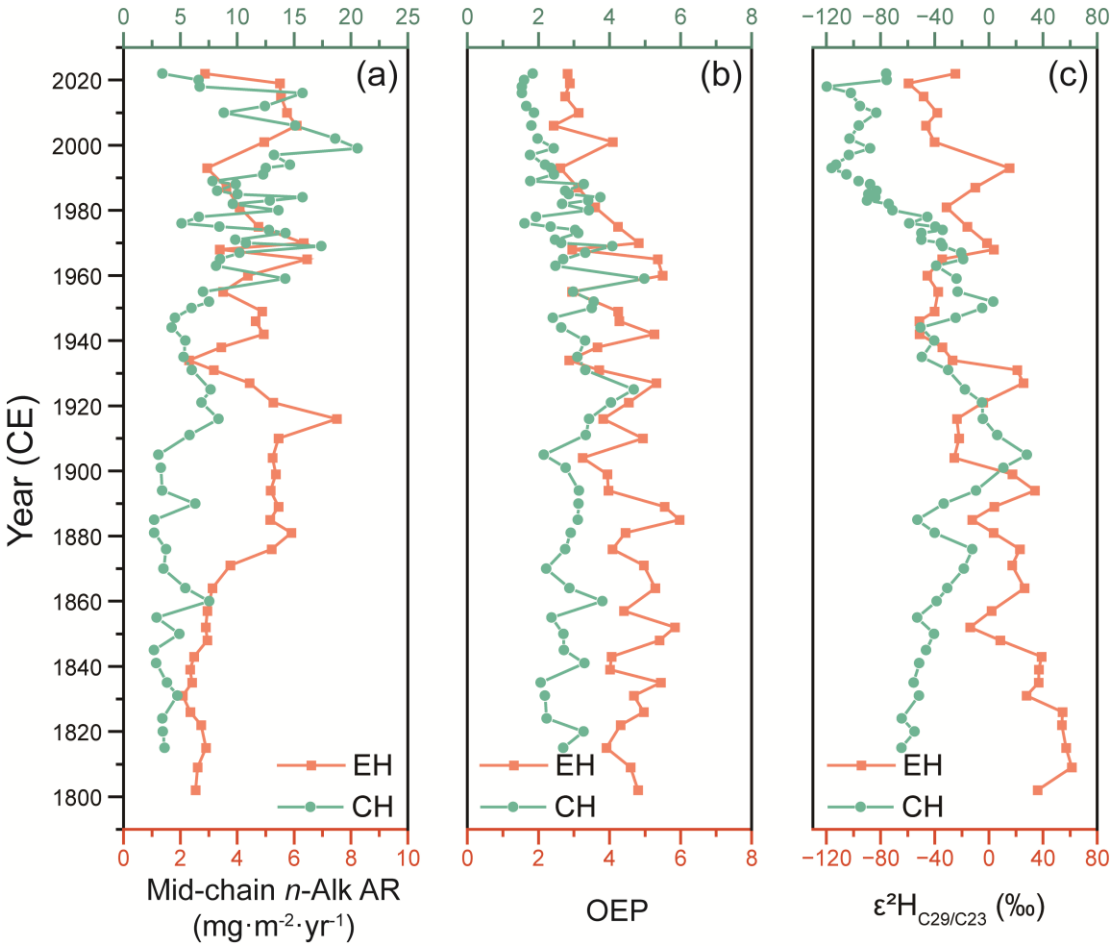

Figure S7. Multi-proxy evidence for mixed sources of mid-chain *n*-alkanes. (a) Persistence of nC_{23}+nC_{25} accumulation in Lake Erhai despite documented aquatic macrophyte decline. (b) Low odd-over-even predominance (OEP) values, consistent with inputs from non-biogenic sources and/or diagenetic alteration. (c) Temporal change in the hydrogen isotope offset between nC_{29} and nC_{23} ($\varepsilon^2H_{C29/C23}$), reflecting a shift in predominant source contributions over time.

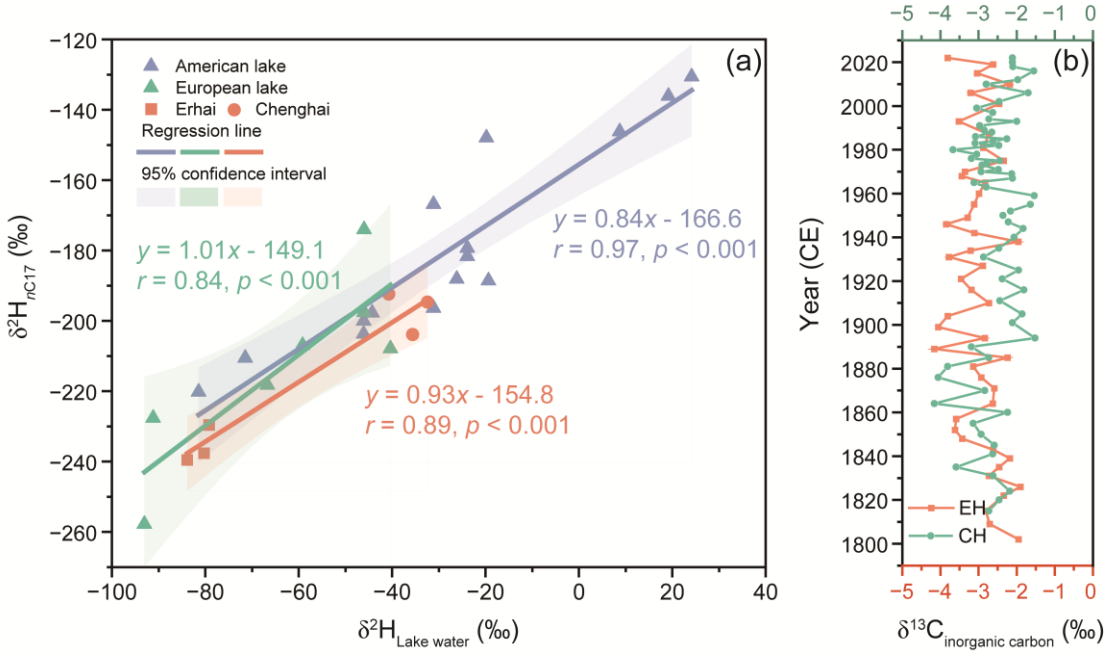

274

275 **Figure S8. Isotopic constraints for defining the aquatic end-member.** (a) Hydrogen isotope
276 fractionation between water and nC_{17} in surface sediments from this study aligns with reported
277 values from global lakes. (b) Stable sedimentary inorganic carbon $\delta^{13}C$ in both lakes, suggesting
278 minimal historical variation in the $\delta^{13}C$ of dissolved inorganic carbon utilized by aquatic plants.

279

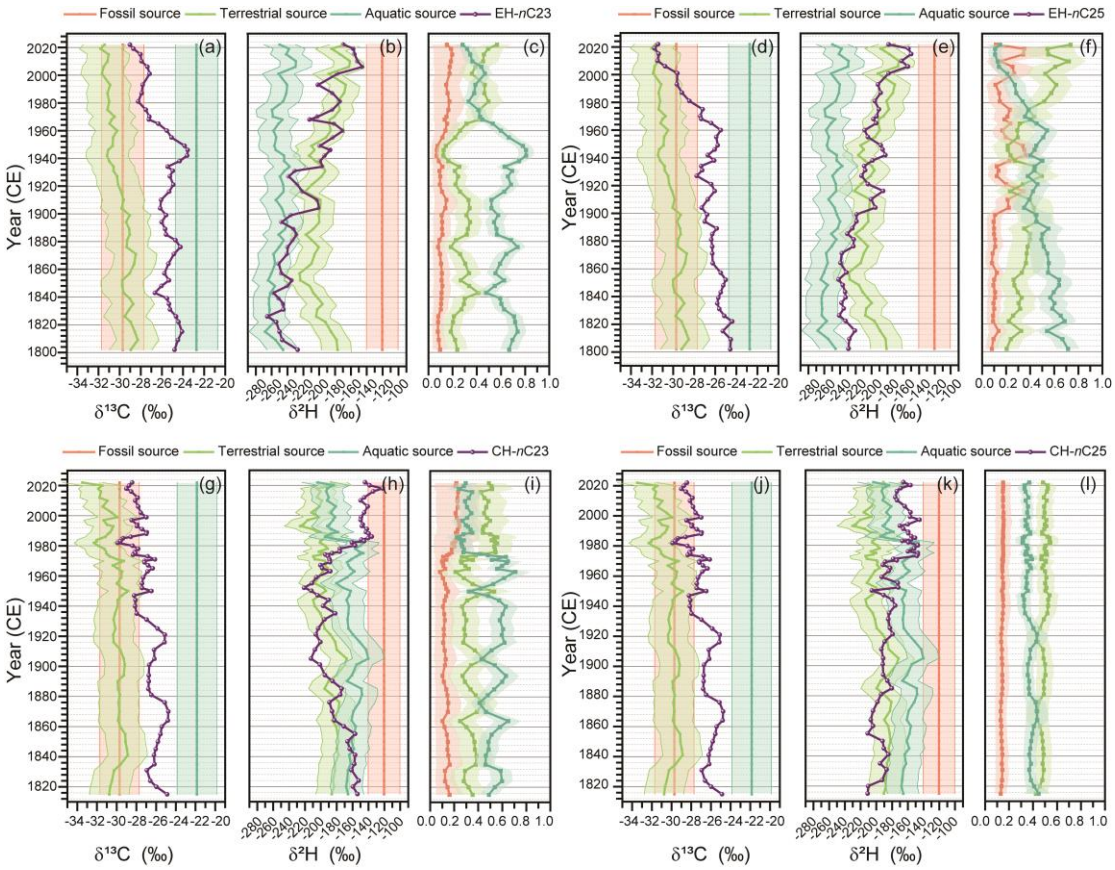

Figure S9. End-member characterization and Bayesian source apportionment of *n*-alkanes in Lakes Erhai and Chenghai. (a, b) $\delta^{13}C$ versus $\delta^{2}H$ of nC_{23} in Lake Erhai (EH) plotted with end-member isotopic ranges. (c) Bayesian-derived source contributions to nC_{23} in EH. (d, e) Same as (a, b) for nC_{25} in EH. (f) Source contributions to nC_{25} in EH. (g, h) $\delta^{13}C$ versus $\delta^{2}H$ of nC_{23} in Lake Chenghai (CH) with end-members. (i) Source contributions to nC_{23} in CH. (j, k) Same as (g, h) for nC_{25} in CH. (l) Source contributions to nC_{25} in CH.

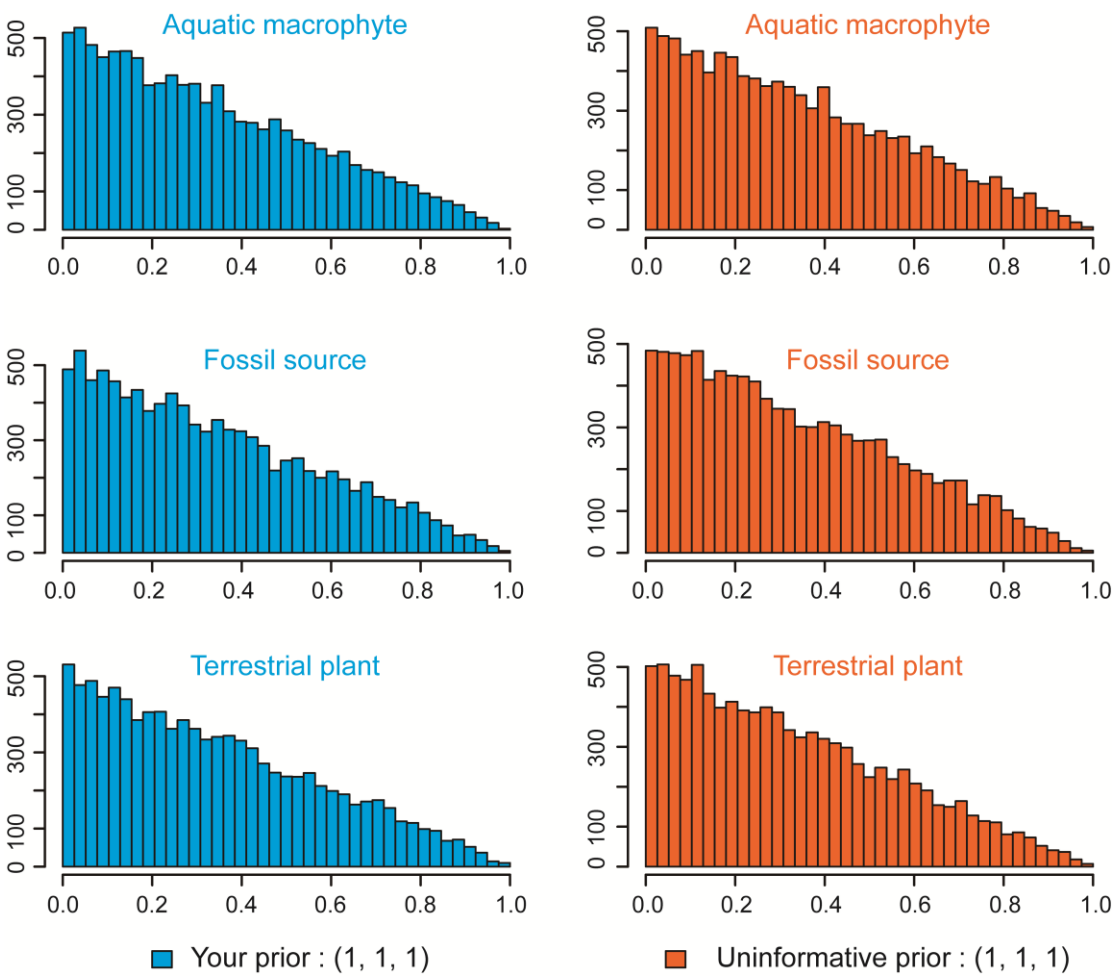

Figure S10. Prior distributions for source proportions in the MixSIAR model. Histograms depict samples drawn from the Dirichlet prior distributions for the three sources: Aquatic macrophyte (top row), Fossil source (middle row), and Terrestrial plant (bottom row). The left panels (blue) show the user-specified prior with parameters (1,1,1), while the right panels (gred) display the default uninformative prior with the same parameters. Both sets exhibit identical marginal distributions, declining from high frequency at low proportions to low frequency at high proportions, indicating a neutral, data-driven modeling approach.

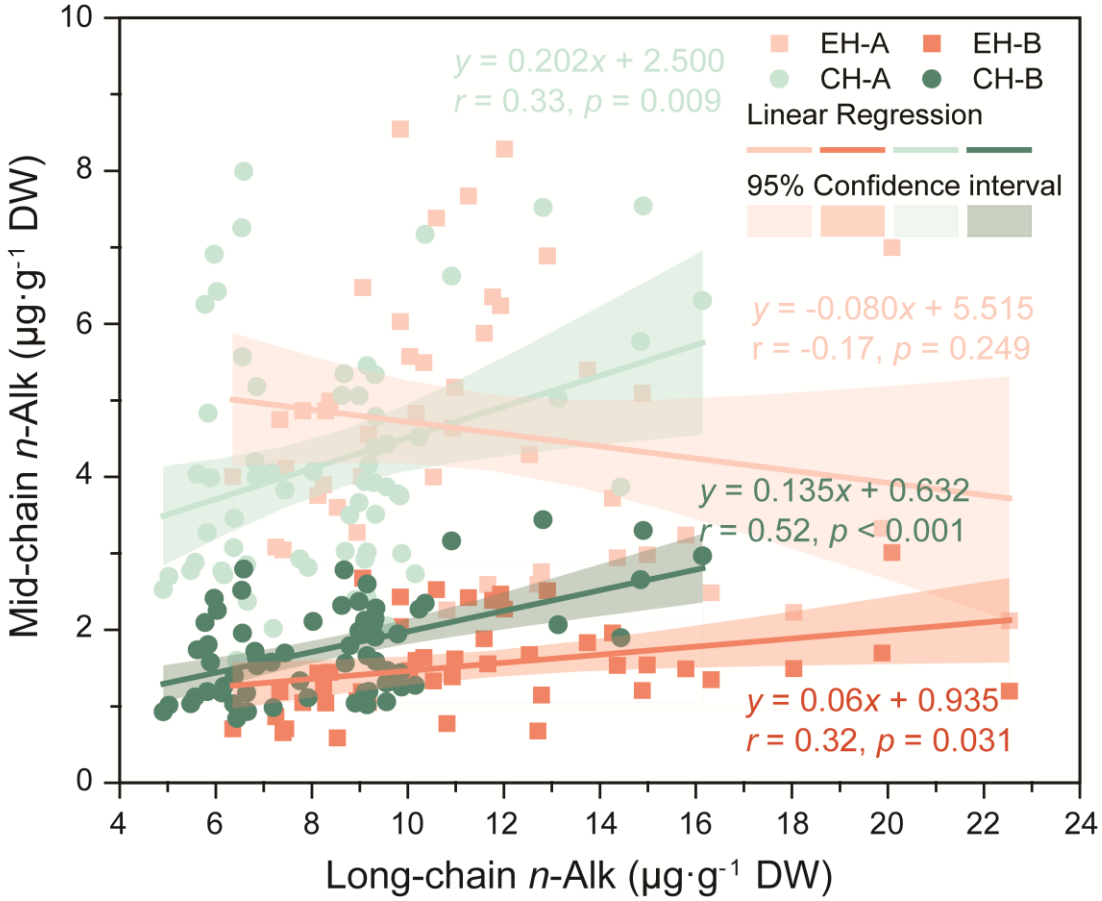

Figure S11. Internal validation of the source-separation achieved by the Bayesian model. Correlation between the terrestrial-plant-derived mid-chain alkane pool (derived post-model) and the long-chain *n*-alkane pool (Ter-*n*Alk) is significantly stronger ($r = 0.32, 0.52$) than the correlation between the total mid-chain alkane pool and Ter-*n*Alk ($r = –0.17, 0.32$). This confirms the model successfully isolated a coherent terrestrial signal from the mixed mid-chain pool.

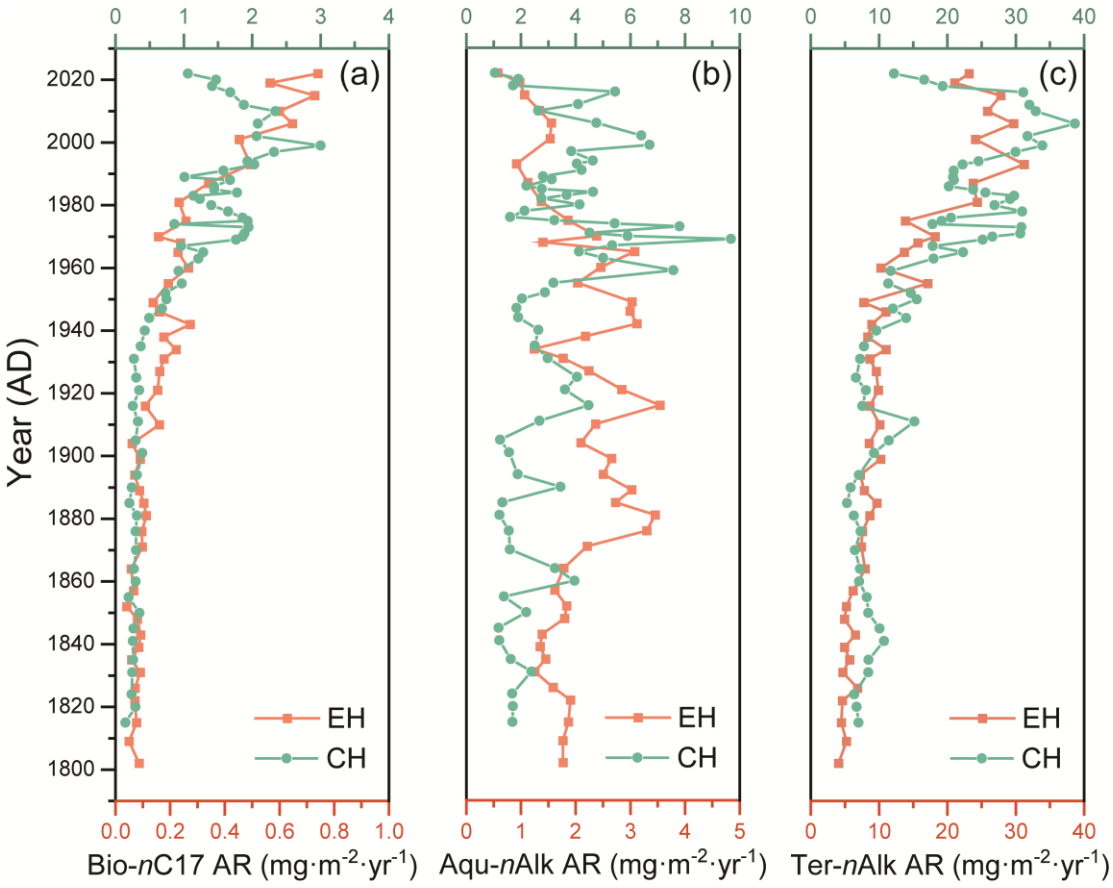

Figure S12. Historical accumulation rates of source-apportioned *n*-alkanes in Lakes Erhai (EH) and Chenghai (CH). (a) Phytoplankton-derived Bio-nC_{17} shows an upward trend toward the present in both lakes. (b) Aquatic macrophyte-derived Aqu-*n*Alk exhibits a marked decline in EH in recent decades. (c) Terrestrial-derived Ter-*n*Alk increases in recent sediments, with superimposed episodic pulses.

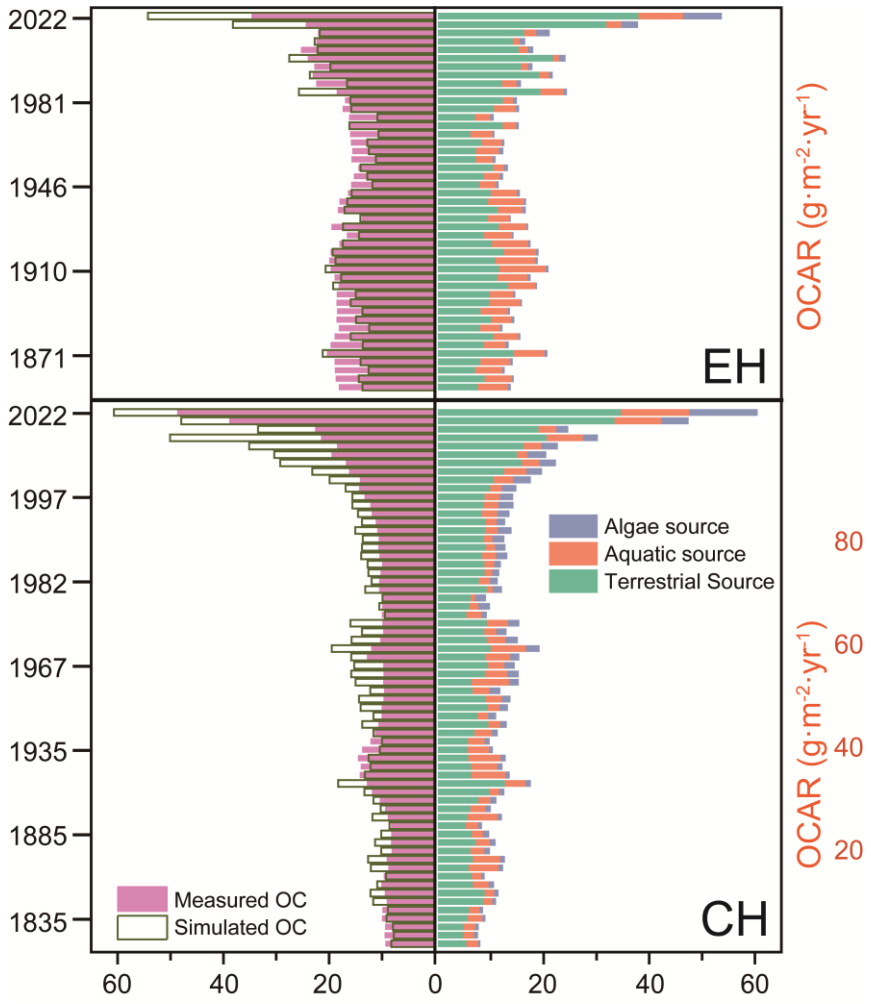

Figure S13. Modelled mineralization and source-specific organic carbon burial in Lakes Erhai and Chenghai. (a) Down-core variations in measured (solid bars) and first-order kinetic mineralization model simulated (open bars) organic carbon (OC) content in Erhai (EH, top) and Chenghai (CH, bottom). Adjacent stacked bars show the modelled proportional contributions to OC from three sources: phytoplankton (light blue), aquatic macrophytes (green), and terrestrial plants (brown).

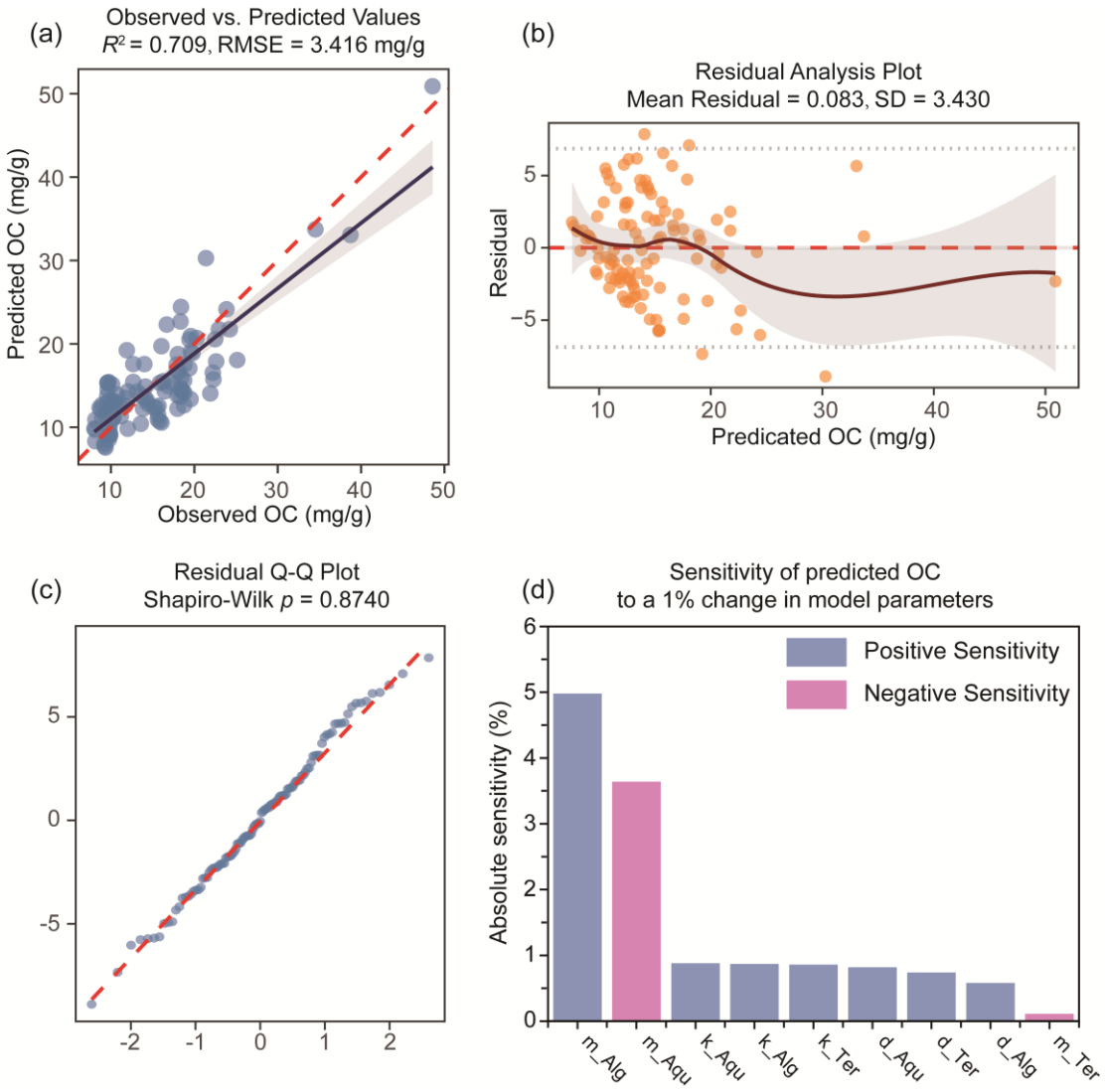

Figure S14. Diagnostic and sensitivity analysis for the first-order mineralization model. (a) Observed versus predicted organic carbon (OC) content. The dashed line indicates 1:1 correspondence (model R^2 = 0.709). (b) Residuals plotted against predicted OC content. The horizontal zero-line shows no systematic bias. (c) Quantile–quantile (Q–Q) plot of residuals. The dashed line represents the expected normal distribution (Shapiro–Wilk p = 0.87). (d) Sensitivity of predicted OC to a ±1 % change in each model parameter. Blue/red bars denote positive/negative responses; all perturbations yielded output changes of < 5 %, supporting model stability.

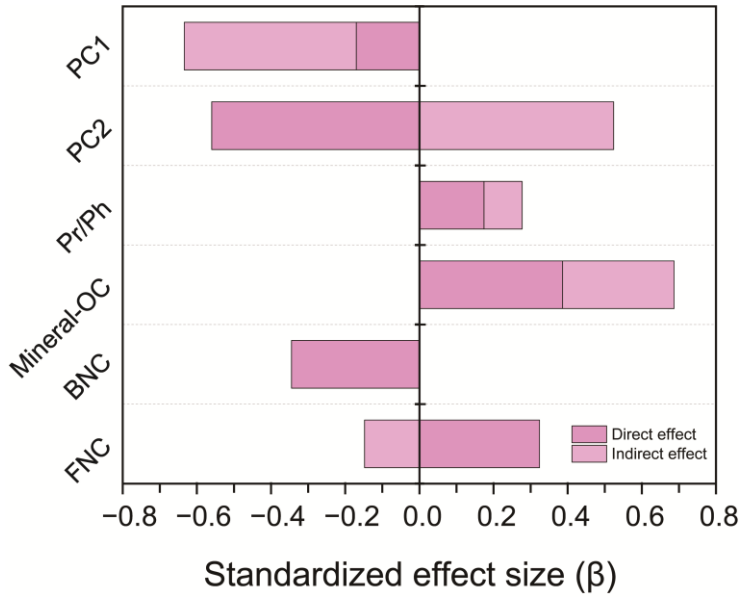

330

331 **Figure S15. Direct, indirect, and total standardized effects of each predictor on burial**
332 **efficiency, derived from the SEM.** Abbreviations: Pr/Ph, Pristane/Phytane ratio; Mineral-OC,
333 mineral-associated organic carbon; BNC, bacterial necromass carbon fraction; FNC, fungal
334 necromass carbon fraction

335

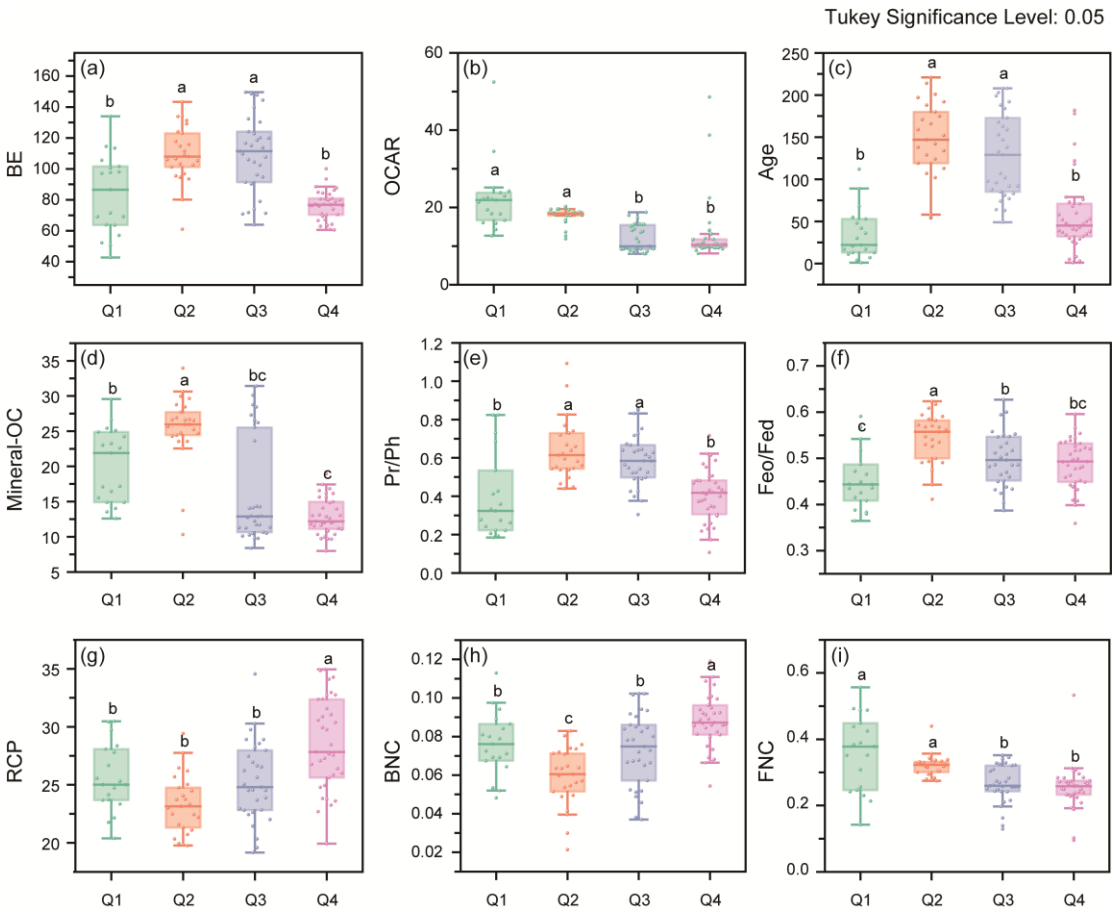

Figure S16. Variations in key sedimentary indicators across PCA-defined source regimes (Quadrants Q1-Q4， Fig. 1e). Boxplots compare the distributions of (a) burial efficiency (BE), (b) organic carbon accumulation rate (OCAR), (c) sediment age (Age), (d) mineral-associated organic carbon (Mineral-OC), (e) Pristane/Phytane ratio (Pr/Ph), (f) reactive free iron to total free iron ratio (Feo/Fed), (g) proportion of recalcitrant carbon pool (RCP), (h) bacterial necromass carbon fraction (BNC), and (i) fungal necromass carbon fraction (FNC) among four quadrants. Letters denote statistically significant differences (Tukey's HSD, $p < 0.05$). Quadrants Q1/Q4 represent phytoplankton-rich regimes (recent eutrophication), and Q2/Q3 reflect macrophyte-dominated states (early natural states).

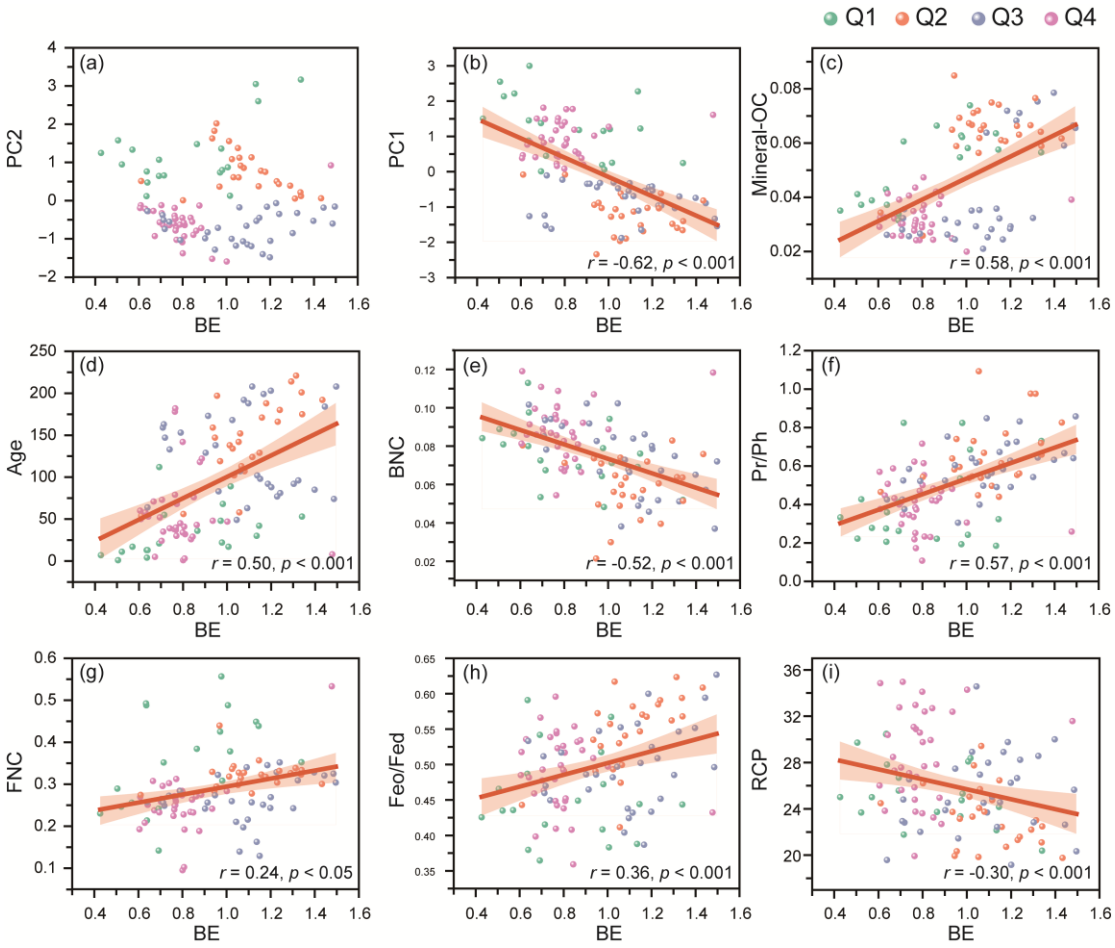

Figure S17. Associations between burial efficiency (BE) and key sedimentary parameters across source regimes. Scatter plots show BE versus (a) PC2 (b) PC1, (c) mineral-associated organic carbon (Mineral-OC), (d) sediment age (Age), (e) bacterial necromass carbon fraction (BNC), (f) Pristane/Phytane ratio (Pr/Ph), (g) fungal necromass carbon fraction (FNC), (h) reactive free iron to total free iron ratio (Feo/Fed) and (i) proportion of recalcitrant carbon pool (RCP). Points are coloured according to the PCA-defined source quadrant (Fig. 1e). Regression lines with 95% confidence intervals are shown per quadrant, illustrating distinct relationships under different source conditions.

Supplementary Tables (Table S1 – S2)

Table S1. Mineralization model diagnostic statistics.

Metric	Value	Interpretation
R^2	0.709	Explains 70.9% variance
Adjusted R^2	0.683	Good fit accounting for predictors
NSE	0.709	Good predictive skill
RMSE	3.416 mg·g^{-1}	Low error relative to mean OC
MAE	2.774 mg·g^{-1}	Average absolute error
MAPE	19.9%	Acceptable relative error
Bias	–0.083 mg·g^{-1}	Minimal systematic error
Residual Mean	0.083	Close to zero
Residual SD	3.430	Moderate spread
Shapiro-Wilk p	0.874	Normally distributed residuals

Table S2. Hierarchical regression blocks and variance explanation.

Block	Variables entered	ΔR^2	Adjusted R^2	F-change	*p*-value
1	PC1	0.387	0.382	68.254	<0.001
2	+ Pr/Ph, Age	0.054	0.425	5.108	0.008
3	+ Feo/Fed, RCP, Mineral-OC	0.108	0.522	8.142	<0.001
4	+ BNC, FNC	0.031	0.547	2.866	0.062

Note: The attenuation of PC1's standardized coefficient from −0.622 (Block 1) to −0.207 (Block 4) indicates mediation by mineral protection and microbial variables.

365

Supplementary References

1. Stock, B. C. *et al.* Analyzing mixing systems using a new generation of bayesian tracer mixing models. *PeerJ* **6**, e5096 (2018).

2. Francis, T. B. *et al.* Habitat structure determines resource use by zooplankton in temperate lakes. *Ecol. Lett.* **14**, 364–372 (2011).

3. Feakins, S. J. *et al.* Production of leaf wax n-alkanes across a tropical forest elevation transect. *Org. Geochem.* **100**, 89–100 (2016).

4. Freimuth, E. J., Diefendorf, A. F., Lowell, T. V. & Wiles, G. C. Sedimentary n-alkanes and n-alkanoic acids in a temperate bog are biased toward woody plants. *Org. Geochem.* **128**, 94–107 (2019).

5. Zhang, Y., Fu, H., Liao, H., Chen, H. & Liu, Z. Geochemical records of lake erhai (south-western China) reveal the anthropogenically-induced intensification of hypolimnetic anoxia in monomictic lakes. *Environ. Pollut.* **299**, 118909 (2022).

6. Zhang, Y., Fu, H., Yang, X. & Liu, Z. Anthropogenically driven changes to organic matter input in sediments of lake chaohu, eastern China, over the past 166 years. *CATENA* **231**, 107285 (2023).

7. Castañeda, I. S. & Schouten, S. A review of molecular organic proxies for examining modern and ancient lacustrine environments. *Quat. Sci. Rev.* **30**, 2851–2891 (2011).

8. Stefanescu, I. C., Macdonald, C., Cook, C. S., Williams, D. G. & Shuman, B. N. Mid- and long-chain leaf wax δ2H values in modern plants and lake sediments from

387 mid-latitude north america. *Geochim. Cosmochim. Acta* **340**, 158–171 (2023).

388 9. Andrae, J. W., McInerney, F. A. & Sniderman, J. M. K. Carbon isotope
389 systematics of leaf wax n-alkanes in a temperate lacustrine depositional environment.
390 *Org. Geochem.* **150**, 104121 (2020).

391 10. Diefendorf, A. F., Leslie, A. B. & Wing, S. L. Leaf wax composition and
392 carbon isotopes vary among major conifer groups. *Geochim. Cosmochim. Acta* **170**,
393 145–156 (2015).

394 11. Zhao, C. *et al.* Paleoclimate Significance of Reconstructed Rainfall Isotope
395 Changes in Asian Monsoon Region. *Geophys. Res. Lett.* **48**, e2021GL092460 (2021).

396 12. Bai, H. *et al.* Compound-specific hydrogen isotope composition of n-alkanes
397 in combustion residuals of fossil fuels. *Atmos. Environ.* **97**, 28–34 (2014).

398 13. Bai, H. *et al.* Stable hydrogen isotope composition of n-alkanes in urban
399 atmospheric aerosols in Taiyuan, china. *Atmos. Environ.* **153**, 206–216 (2017).

400 14. Yamamoto, S. & Kawamura, K. Application of urea adduction technique to
401 polluted urban aerosols for the determination of hydrogen isotopic composition of *n* -
402 alkanes. *Int. J. Environ. Anal. Chem.* **92**, 302–312 (2012).

403 15. Wang, P. *et al.* Stable carbon isotopic characteristics of fossil fuels in China.
404 *Sci. Total Environ.* **805**, 150240 (2022).

405 16. Tang, T. *et al.* Source Diversity of Intermediate Volatility *n* -Alkanes Revealed
406 by Compound-Specific δ^{13} C−δD Isotopes. *Environ. Sci. Technol.* **56**, 14262–14271
407 (2022).

17. Bush, R. T. & McInerney, F. A. Leaf wax n-alkane distributions in and across modern plants: implications for paleoecology and chemotaxonomy. *Geochim. Cosmochim. Acta* **117**, 161–179 (2013).

18. Strobel, P. *et al.* Precipitation and Lake Water Evaporation Recorded by Terrestrial and Aquatic *n* -Alkane δ^2 H Isotopes in Lake Khar Nuur, Mongolia. *Geochem. Geophys. Geosystems* **23**, e2021GC010234 (2022).

19. Liu, J. & An, Z. Leaf wax n-alkane carbon isotope values vary among major terrestrial plant groups: different responses to precipitation amount and temperature, and implications for paleoenvironmental reconstruction. *Earth-Sci. Rev.* **202**, 103081 (2020).

20. Gao, L., Hou, J., Toney, J., MacDonald, D. & Huang, Y. Mathematical modeling of the aquatic macrophyte inputs of mid-chain n-alkyl lipids to lake sediments: implications for interpreting compound specific hydrogen isotopic records. *Geochim. Cosmochim. Acta* **75**, 3781–3791 (2011).

21.Mügler, I. *et al.* Effect of lake evaporation on δD values of lacustrine n-alkanes: a comparison of nam Co (tibetan plateau) and holzmaar (germany). *Org. Geochem.* **39**, 711–729 (2008).

22. Sachse, D., Radke, J. & Gleixner, G. Hydrogen isotope ratios of recent lacustrine sedimentary n-alkanes record modern climate variability. *Geochim. Cosmochim. Acta* **68**, 4877–4889 (2004).

23. Garcin, Y. *et al.* Hydrogen isotope ratios of lacustrine sedimentary n-alkanes

as proxies of tropical african hydrology: insights from a calibration transect across cameroon. *Geochim. Cosmochim. Acta* **79**, 106–126 (2012).

24. Wang, Y. *et al.* Evaporation dominates the loss of plateau lake in Southwest China using water isotope balance assessment. *Sci. Total Environ.* **873**, 162415 (2023).

25. Pronin, E., Panettieri, M., Torn, K. & Rumpel, C. Stable carbon isotopic composition of dissolved inorganic carbon (DIC) as a driving factor of aquatic plants organic matter build-up related to salinity. *Ecol. Indic.* **99**, 230–239 (2019).

26. Song, C. *et al.* Spatiotemporal variability and sources of DIC in permafrost catchments of the Yangtze River source region: insights from stable carbon isotope and water chemistry. *Water Resour. Res.* **56**, e2019WR025343 (2020).

27. Quanliang, J. *et al.* New perspectives on organic carbon storage in lake sediments based on classified mineralization. *CATENA* **237**, 107811 (2024).